NGC 4314. II. *HUBBLE SPACE TELESCOPE I*-BAND SURFACE PHOTOMETRY OF THE NUCLEAR REGION

G. F. Benedict

McDonald Observatory, University of Texas, Austin, Texas 78712

J. L. Higdon,[1] W. H. Jefferys, R. Duncombe, P. D. Hemenway, P. J. Shelus,
A. L. Whipple, E. Nelan, D. Story, B. McArthur, and J. McCartney

Astronomy Department, University of Texas, Austin, Texas 78712

O. G. Franz

Lowell Observatory, Mars Hill Rd., 1400 W., Flagstaff, Arizona 86001

L. W. Fredrick

Department of Astronomy, University of Virginia, Charlottesville, Virginia 22903

Wm. F. van Altena

Astronomy Department, Yale University, P.O. Box 6666, New Haven, Connecticut 06511
Received 1992 July 23; revised 1992 December 17

ABSTRACT

We present a *Hubble Space Telescope I*-band Planetary Camera image of the nuclear region of NGC 4314. This is an anemic barred galaxy with recent star formation confined to a nuclear ring. These data resolve the nuclear ring into multiple sites of new star formation and resolve associated dust lanes into discrete clouds. Unsharp masking of a Lucy–Richardson deconvolved image reveals a strong spiral dust pattern. Deconvolution results in at least 0.13 arcsec resolution, as demonstrated by the de Vaucouleurs $r^{1/4}$ law. Contrasted with similar studies of M87 and NGC 7457, we find no photometric evidence for an extreme concentration of stars in the center of NGC 4314. We identify an oval distortion of length 8 arcsec in the nuclear region, using ellipse-fitting routines and the unsharp masked frame. This nuclear bar has newer stars near its ends. We catalog 14 star clusters associated with H II regions in the nuclear ring. As an additional demonstration of the resolution achieved, the integral size distribution of these clusters is described by an exponential relationship which prevails down to 0.14 arcsec.

1. INTRODUCTION

In this second paper in a series concerning NGC 4314 [SB(rs)ap] we present a higher-resolution view of its complex nuclear morphology. We have summarized previous work at all wavelengths in Benedict *et al.* (1992, hereafter Paper I). Broadband optical and short-wavelength IR (Paper I), Hα (Pogge 1989), and radio continuum (Garcia-Barreto *et al.* 1991) imagery reveals a nuclear ring composed of recently formed stars. The fundamental mechanism driving the formation and maintenance of a nuclear ring seems reasonably well understood (Combes & Gerin 1985) in broad outline. Rings are a consequence of orbital resonances, with nuclear rings forming at an Inner Lindblad Resonance (ILR). There are many details in the distribution and motions of stars, dust, and gas in and near the nuclear ring in NGC 4314 that raise questions about this simple model. A simple bar resonance may be an insufficient mechanism.

We wish to examine the detailed *I*-band morphology of the star formation sites in NGC 4314. The expectation is that these *Hubble Space Telescope* data will provide some observational constraints and clues as to which star formation mechanism discussed in Paper I is operating in the nucleus of NGC 4314.

We use Lucy–Richardson deconvolution to remove some of the deleterious effects of *HST* spherical aberration, and apply unsharp masking so that shapes and distributions of dust and star clusters can be studied. Applying these techniques has allowed us to map the dust and stellar associations comprising the nuclear ring in great detail, but still with somewhat less resolution than originally anticipated.

In this paper we shall briefly discuss the data acquisition, reduction process, and resulting data quality in Sec. 2. In Sec. 3 we outline the technique used to deal with the spherical aberration affecting *HST*. We derive a photometric calibration in Sec. 4. The results of our explorations of these data are given in Sec. 5, where we discuss the detailed morphology of the ring and nucleus. We also model the nuclear bulge and determine the spatial and size distributions of the star clusters associated with the nuclear ring

[1]Now at National Radio Astronomy Observatories, Socorro, NM 87801.

H II regions. Section 6 presents a brief discussion and our conclusions.

Doubts concerning deconvolution and the preservation of photometric scales led us to restrict our initial observations to a single bandpass. We discuss no new color information in this paper.

Assuming $D = 10$ Mpc (Garcia-Barreto *et al.* 1991), 1 arcsec corresponds to 48.5 pc.

2. THE DATA

As discussed in Paper I, the *I* bandpass, in the near-infrared, indicates the location of the "most effective" (largest optical depth) dust. However, the stellar associations underlying the H II regions are still apparent, especially in the unsharp masked frames [see Paper I, Fig. 18(a)]. These considerations prompted our choice of the

F785LP filter. The filter, a Johnson *I*-band equivalent, has a FWHM of 800–1010 nm (Griffiths 1990).

These data were acquired 1991 April 29 with the *HST* WFPC Planetary Camera (PC), a mosaic of four 800 ×800 pixel TI CCDs. Our data set consists of two 200 s F785LP exposures. We preflashed the CCDs before each exposure. The pixel size for the PC is 0.043 arcsec, or 2.1 pc. Guiding was in Coarse Track mode. Inspection of the guide star jitter indicated pointing stability of better than 0.03 arcsec. The images of all four CCDs from the two PC frames were corrected for analog-to-digital (A/D) errors, bias subtracted, and flat fielded in the standard STScI pipeline (Lauer 1989). Finally, bad columns were replaced by linear interpolation and the cosmic ray events removed by deleting large single-pixel events not present in both images. The nucleus and the associated region of nuclear star formation are almost completely contained within the con-
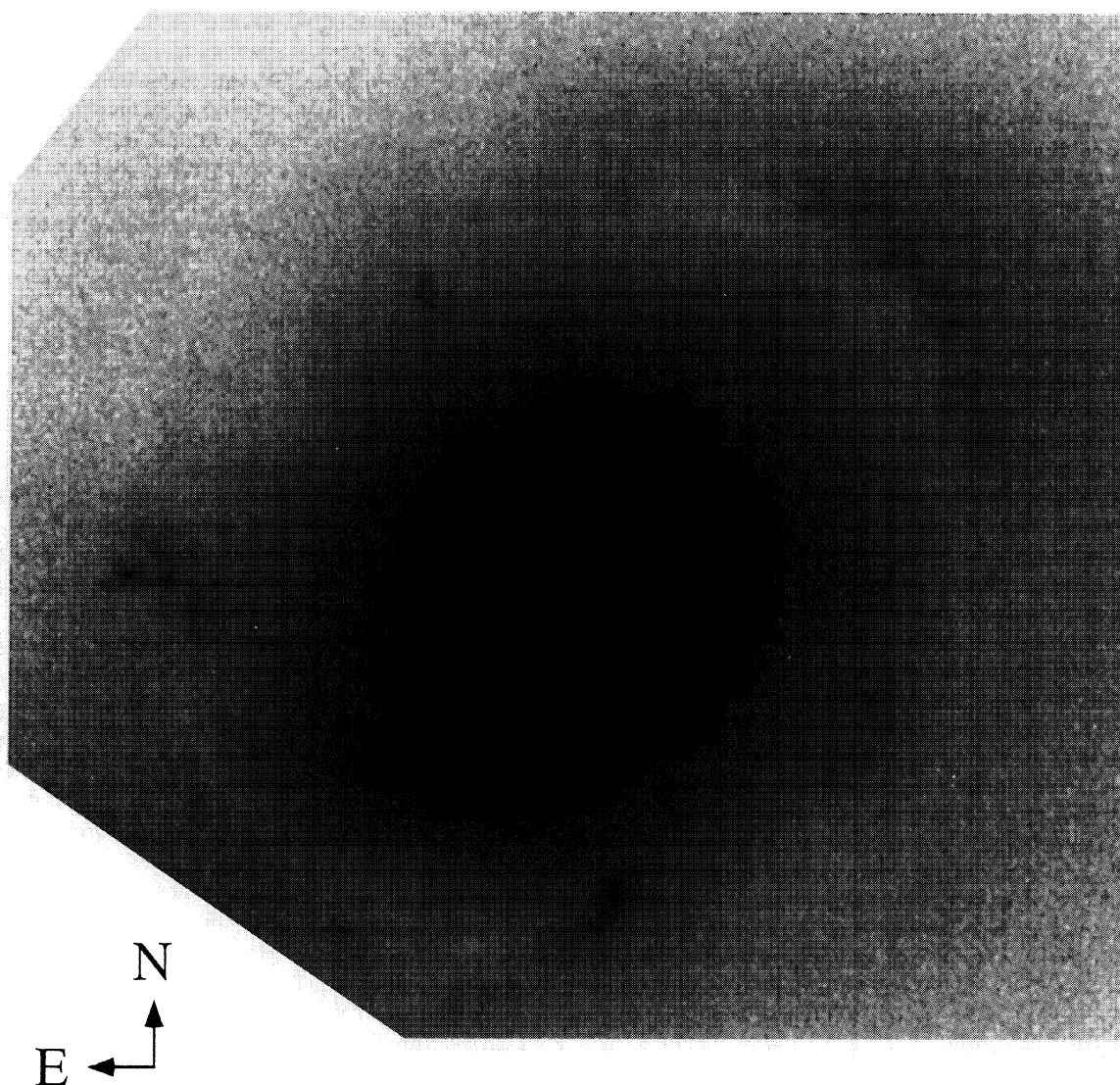

FIG. 1. Nucleus of NGC 4314. Sum of two F785LP (*I*-band) 200 s exposures with PC6. Pixel size is 0.043 arcsec. The direction arrows have a length of 1.0 arcsec. The effects of spherical aberration include filling in the dust lanes and smearing the details in the nuclear ring.

fines of one of the four CCDs, PC6. At this scale and integration time, sky background is negligible. Image motion between the two frames was less than half a pixel. Hence, we simply coadded the frames.

Our final co-added PC6 frame is presented in Fig. 1. The grayscale stretch was chosen to highlight the ring of star formation. This array provides per pixel S/N = 19 for *I*-band surface magnitude $\mu_I \leqslant 17.5$ (units are magnitude per square arcsec). The noise in Fig. 1 is Poisson for $\mu_I \leqslant 17.5$. At $\mu_I = 18.5$, the per pixel S/N = 7. We discuss the calibration that produces these magnitude levels and we provide a surface magnitude contour map (Fig. 5) in Sec. 4. Readout noise was determined to be 2.6 ADU (analog-to-digital units).

3. IMAGE PROCESSING

These data are blurred by spherical aberration introduced by the *HST* primary mirror (Burrows *et al.* 1991).

In this section we discuss our use of a (by now standard) deconvolution technique suitable for restoring the resolution of the *HST* images to an almost unaberrated condition. For our deconvolution, we have ignored known point spread function (PSF) changes from one part of PC6 to another. To enhance the morphological detail in these exposures, we utilize unsharp masking.

3.1 Deconvolution

We deconvolved a 512×512 pixel subset of the combined PC6 data with a Lucy (1974) code, using a stellar PSF derived from a model of the *HST* optics corresponding to the secondary mirror position on the date of observation. We chose 20 iterations based on the experience of Lauer *et al.* (1991) with NGC 7457. As pointed out in Burrows *et al.* (1991) a model PSF is unaffected by jitter-induced blurring. Additionally, the model is noise free.
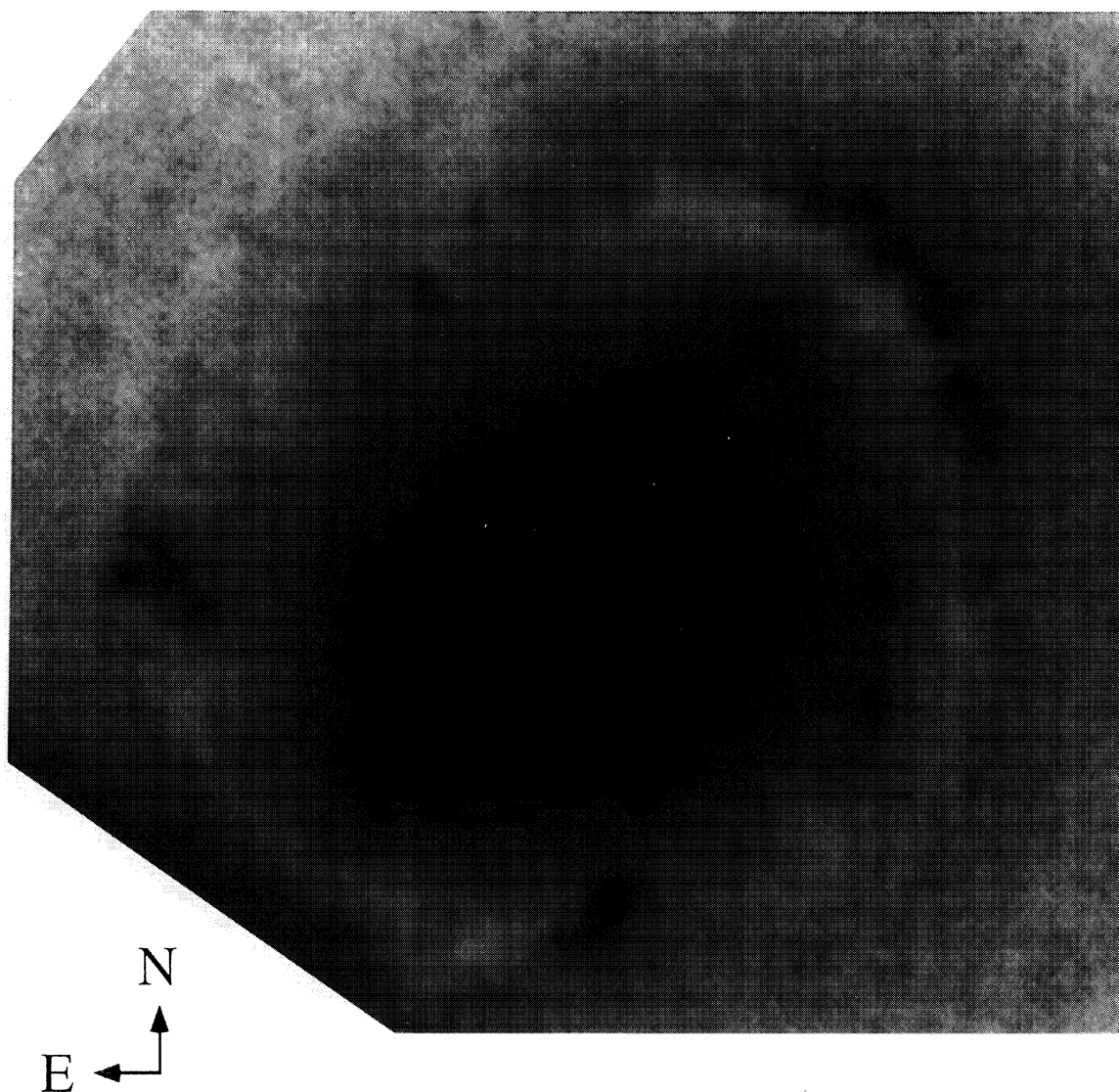

FIG. 2. Same as Fig. 1 subjected to 20 iterations of a Lucy–Richardson deconvolution with a model PSF. Same grayscale stretch as Fig. 1. Note the increased definition of the dust lanes and of the star clusters in the nuclear ring.

These attributes, along with the agreement of their models with observed PSF for single stars, prompted our use of a model PSF for deconvolution. We present our deconvolved data in Fig. 2. The grayscale stretch is the same as for Fig. 1. Note the increased depth in the dust lanes and that the sites of new star formation in the ring are more sharply defined.

3.2 Unsharp Masking

The utility of unsharp masking has been discussed in Paper I. Unsharp masking emphasizes regions of rapid change of brightness, that is, regions where conditions of extinction and/or stellar clumping are changing on short distance scales. Unsharp masking is equivalent to a high-pass filtering process. Figure 3 displays the *I*-band unsharp masked frame, I_{hp}, for the Lucy deconvolved data from

PC6. The low-pass array used in the masking procedure was produced by convolving the original Lucy deconvolved *I* data with a 2D Gaussian with $\sigma = 1$ arcsec. The star clusters and dust clouds are seen more clearly in Fig. 3 than in Fig. 2. Since each star cluster is not completely surrounded by a valley, we have not introduced significant structure induced by ringing.

4. CALIBRATION

Figure 4 compares ground-based calibrated surface photometry (Paper I) against the deconvolved *HST I*-band data for an average profile through the center of the galaxy at PA = 58°. The ground-based data are in magnitudes per square arcsec and were obtained with a Cousins *I* filter. The *HST* data is in units of instrumental magnitudes per
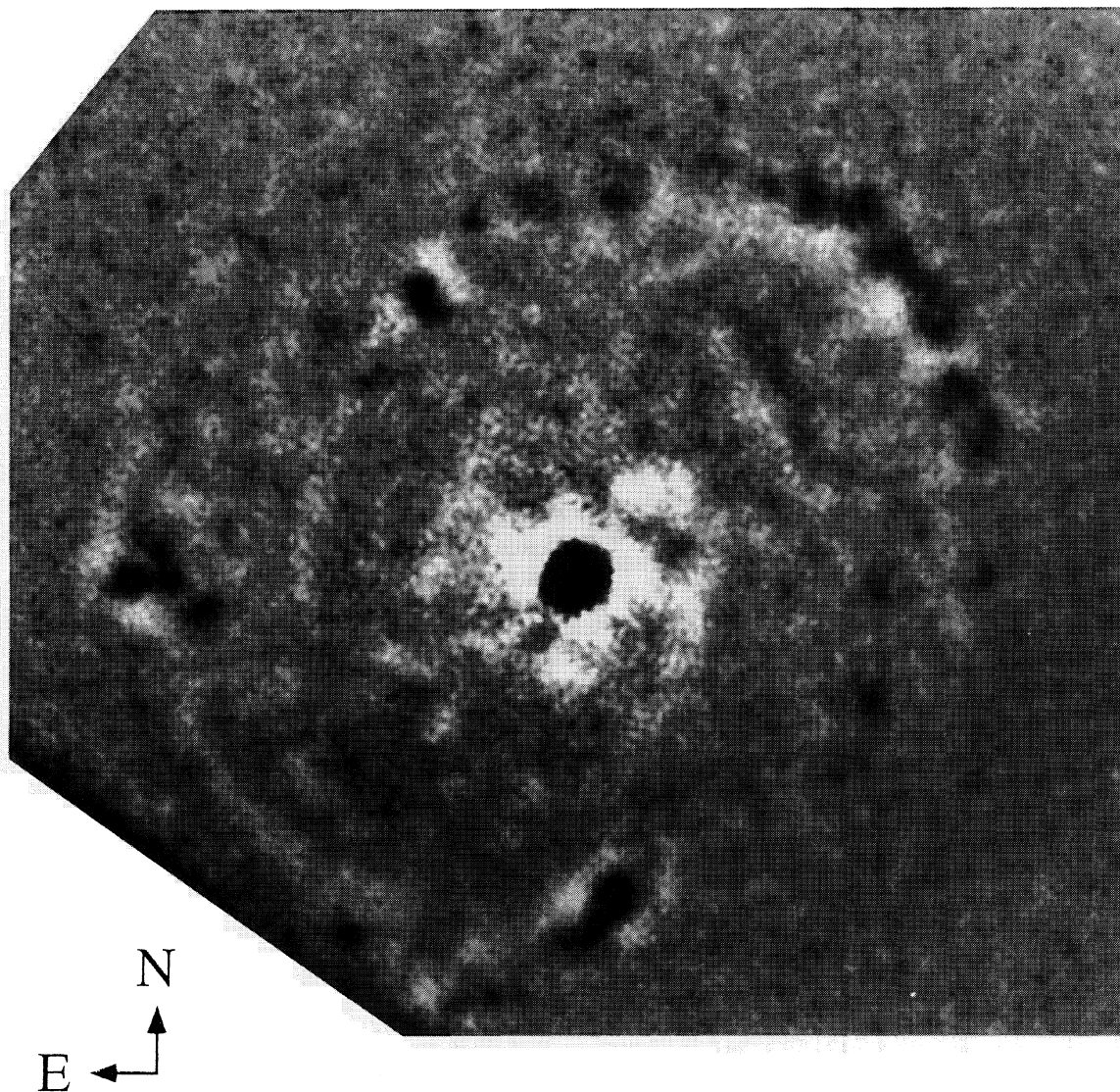

FIG. 3. The data from Fig. 2 unsharp masked using a 1 arcsec Gaussian smoothing kernel. The whitest regions are 10 ADU above the local mean. The darkest regions are 10 ADU below the local mean. The frame edges are affected by flat fielding deficiencies, especially to the SE and NW.
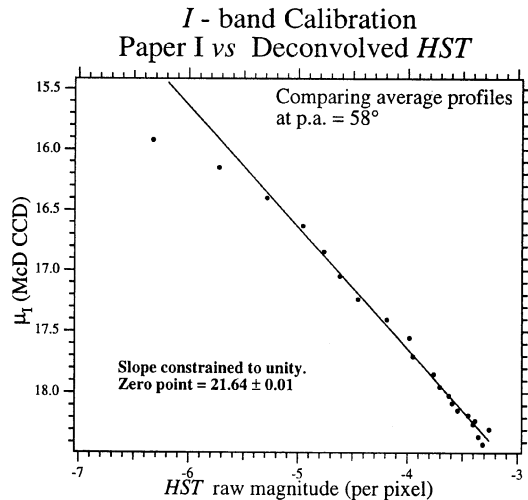
I - band Calibration
Paper I *vs* Deconvolved *HST*

FIG. 4. Comparison of Paper I *I* surface magnitudes with per pixel surface magnitudes generated from Fig. 2. The relationship breaks down at the bright end because of the poorer resolution of the Paper I data. The solid line is the best fit to the data with μ_I (McD CCD)$\geqslant 16.4$.

pixel. As noted before, the *HST* data are acquired through a filter closely approximating a Johnson *I*. From Paper I we find a maximum range $0.9 < V - I < 1.2$ in the region presented in Fig. 2. Using the *I*-band transformations of Bessel (1979), we predict a maximum difference of I(Johnson)$-I$(Cousins)$=0.09$ due to color variations. In the two-magnitude range covered by the average profiles, correspondence is good, the average residual being 0.04 mag. Resolution deficiencies in the ground-based data become apparent for $\mu_I \leqslant 16.4$. The faint limit for the calibration is imposed by the limited areal coverage of PC6.

Figure 5 provides a surface magnitude contour map, calibrated using the relationship displayed in Fig. 4. The contoured region is equivalent to the grayscale map of Fig. 2. The H II regions (knot A and B) identified in Wakamatsu & Nishida (1980) are also labeled.

5. RESULTS

In this section we first identify the components detectable in Fig. 2, then search for patterns in the morphology of the nuclear region. We next model the nuclear bulge and extend the $r^{1/4}$ relationship found in Paper I further into the nucleus. Then we turn to the star clusters associated with the H II regions (Pogge 1989), and determine a size distribution.

5.1 Morphology of the Nuclear Region

We begin by urging a comparison of the best ground-based I_{hp} data from Paper I [Fig. 18(a)] and Fig. 2, our Lucy–Richardson deconvolution of the PC6 data. Remarkably, most of the details in the ground-based data are confirmed. The dust lanes were patchy and the ring of star formation partially resolved into clusters in Paper I. The

impression of a barlike distribution interior to the ring was strong, but thought in Paper I to be an artifact of absorption by the nearby dust lanes.

5.1.1 The core of the nucleus

The *JHK* short-wavelength IR photometry of Paper I (Fig. 9) revealed a nuclear bar at PA$=0°$ and length 2 arcsec at the $\mu J = 15.00$ level. It was not seen in Paper I in μ_I, nor was it seen in more recent *K*-band observations (Combes *et al.* 1992). Neither does the present higher resolution imagery show this bar. In Paper I we found $\mu_{I-J} = 1.05$ for the nucleus. Therefore, if visible in *I*, we should detect this bar in the present *HST* data at the $\mu_I = 16.05$ level. The $\mu_I = 16.0$ contour in Fig. 5 perhaps shows a slight NS extension. However, fitting ellipses to the deconvolved intensity data (using the algorithms of Jedrzejewski 1987) provides no confirmation of the existence of this bar. Parameters for the fit ellipses are presented in Fig. 6. It is likely that the nuclear bar seen in Paper I was an artifact produced by the camera.

5.1.2 Other barlike structures

NGC 4314 is classified SB(rs)ap. The bar prompting this classification is obvious on the Palomar Observatory–National Geographic Sky Survey plates at PA$=148°$, length ~ 120 arcsec. We shall denote this bar$_1$.

The nucleus contains another barlike structure. The ellipses fit to the *HST I* data and shown in Fig. 6 exhibit a region of changing ellipticity, ϵ, in the range $2.4 \leqslant a \leqslant 3.5$ arcsec. Also, the *HST* I_{hp} data (Fig. 3) and the surface magnitude contour map (Fig. 5, $\mu_I = 17.25$ level) give the weak impression of a barlike distribution in this range. We call this bar$_2$. As discussed by Jedrzejewski (1987), the third and fourth harmonics describe either boxy or spindle deviations from a pure ellipse. The errors obtained for the third and fourth harmonic parameters from the ellipse fits were large compared to their near-zero values in this range. Hence we have no numerical confirmation of either a spindle or boxy bar.

Bar$_2$ was detected in the ground-based data discussed in Paper I [Fig. 18(a)], but was attributed to the masking effects of the dust lanes. Now that the dust lanes are resolved (e.g., Fig. 3), we find no masking effect. Hence, we identify bar$_2$ as a stellar distribution.

The *HST* I_{hp} data (Fig. 3) seem to indicate stellar clustering interior to the ring, especially at the ends of bar$_2$. These may be newer stars. We obtain some support for this interpretation from the ground-based surface colors presented in Paper I. Figure 7 presents a comparison between μ_I from the *HST* data and μ_I from Paper I, obtained from profiles through the nucleus at PA$=148°$, along the axis of bar$_1$. We also plot $V - K$ colors from Paper I. Structure interior to the nuclear ring includes groups of newer stars (the ground-based color indices drop slightly at the relevant positions) and lanes of dust, both near the ends of the nuclear bar. If a real structure, this bar has a length of 350 pc at PA$=145°$.

NGC 4314
Calibrated Surface Magnitudes
HST μ_I

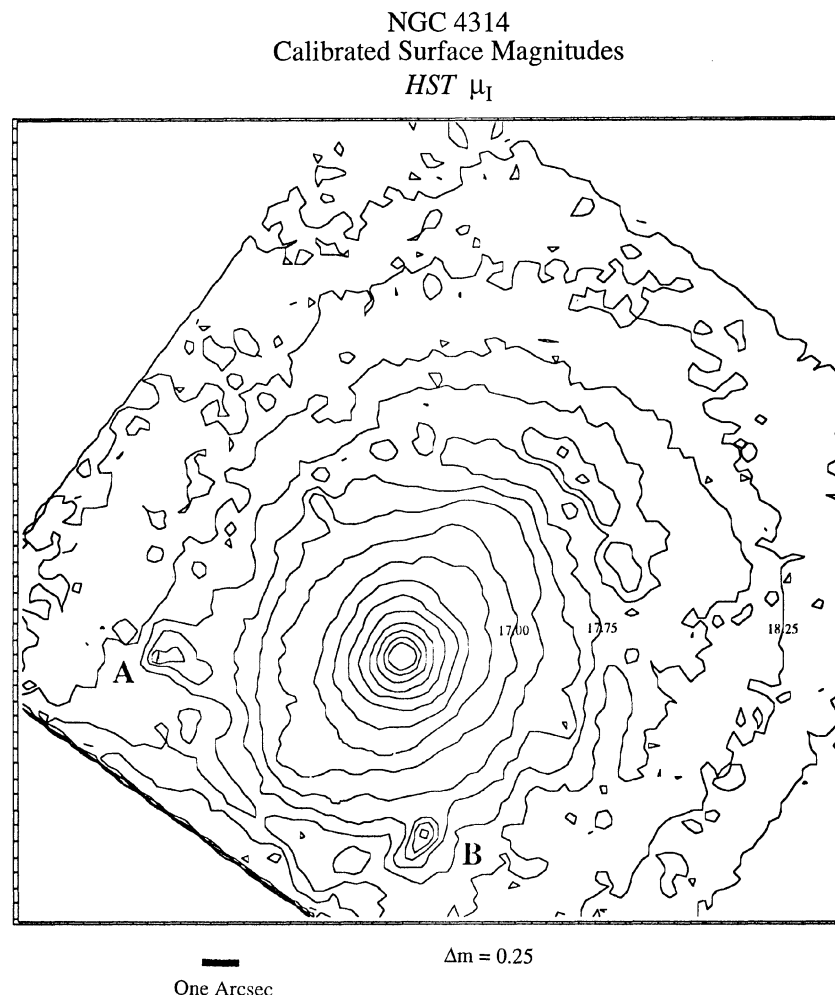One Arcsec $\Delta m = 0.25$

FIG. 5. Contour map of the calibrated μ_I obtained for each pixel in Fig. 2, using Fig. 5. The contours are separated by 0.25 mag. Three contour levels are labeled to the right of the nucleus. Also identified are knots A and B from Wakamatsu & Nishida (1980).

5.1.3 *The nuclear ring*

The nuclear ring contains dust (identified photometrically in Paper I) now resolved into discrete clouds and star clusters associated with the H II regions (identified in Pogge 1989). From Fig. 3 the nuclear ring is a nuclear spiral, especially as delineated by the dust distribution. We see a two-arm spiral of dust and star clusters. The largest clouds appear to be associated with the largest star clusters. This is apparent in both the deconvolved and unsharp masked images and so is not simply a processing artifact. This spiral is not uniformly populated with either dust clouds or star clouds. Note also the tendency for star clusters to lie outside the strings of discrete dust clouds. Table I in Sec. *5.3* catalogs the star clusters associated with the nuclear H II regions.

5.2 *Modeling the Nuclear Bulge*

Figure 8 presents an average luminosity profile perpendicular to bar_1 (PA=58°) plotted against $r^{1/4}$, derived from the *HST I* data after deconvolution. Since each data

point in Fig. 8 is the result of two four-point interpolations, the errors associated with the faintest levels are less than 0.05 mag. In Paper I we found an $r^{1/4}$ distribution only to our resolution limit of $r \sim 2$ arcsec. This profile is also plotted in Fig. 8. We see that deconvolution of the *HST* data has extended the range of agreement with the de Vaucouleurs $r^{1/4}$ relationship for the nuclear bulge inward to a limit of 0.13 arcsec. The ground-based and *HST*-derived $r^{1/4}$ relationships are identical within the errors.

We also present a comparison with NGC 7457, an elliptical galaxy known to contain a stellar cusp (Lauer *et al.* 1991). The actual observation times were 160 s per frame for NGC 7457 rather than the published 400 s (Lauer 1992). Thus, the S/N for our data should be somewhat higher and should tolerate more deconvolution iterations. Nonetheless, we chose 20 iterations so that these deconvolved data (Fig. 2) are directly comparable to NGC 7457. The distances to each galaxy are also similar. Lauer *et al.* 1991 estimate $D=12.5$ Mpc for NGC 7457.
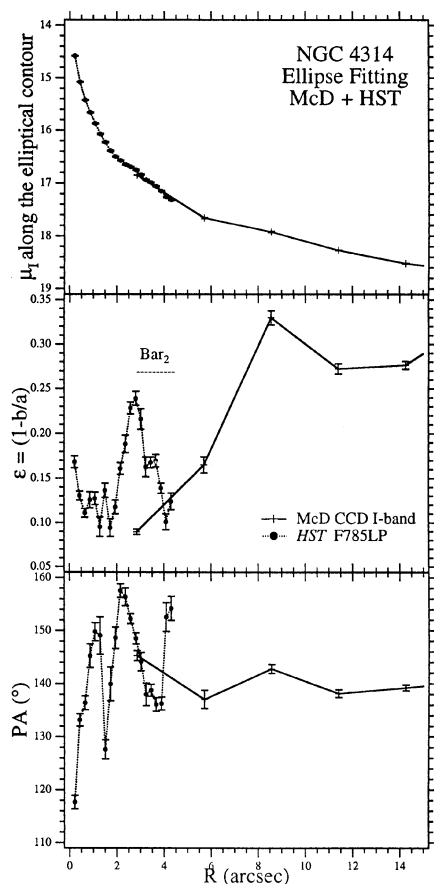
Plotting (Fig. 8) the NGC 7457 Lucy deconvolved *V*

FIG. 6. Average surface magnitude $\langle\mu_I\rangle$, position angle, and ellipticity as a function of semi-major axis for ellipses fitted to Fig. 2 I surface intensities. Bar$_2$ is obvious in ellipticity as $r=3$ arcsec. We also plot lower resolution data from Paper I. All error bars are $1-\sigma$.
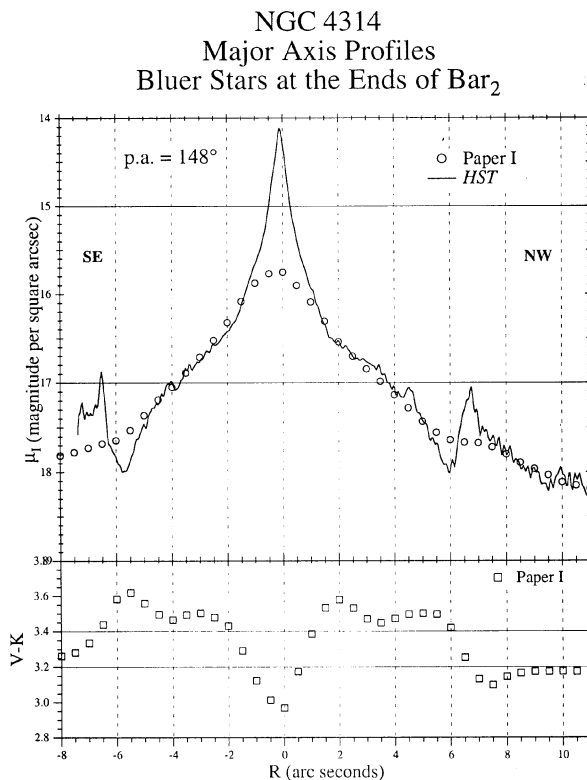

FIG. 7. Detailed *HST* and Paper I surface magnitude profiles, demonstrating the superior resolution of the *HST* data. The $V-K$ color profile is from Paper I. We see evidence of color changes (at $r=\pm4$ arcsec) associated with the ends of bar$_2$.

data as a function of $r^{1/4}$ shows it to have a completely different behavior than the NGC 4314 profile. The inner cusp of NGC 7457 pushes the profile well above the $r^{1/4}$ relationship. Lastly, subjecting the raw NGC 7457 frames to unsharp masking reveals a faint, but unmistakably PSF-like distribution at the nucleus. We see no such signature in the unsharp masked raw NGC 4314 data. Hence, the nucleus of NGC 4314 appears resolved and contains no extreme concentration of stars.

5.3 Star Clusters Associated with H II Regions: Diameters and Luminosities

Our data show numerous star clusters in the ring. As an example of the increased resolution provided by *HST*, Fig. 9 presents a comparison between an I contour map based on data presented in Paper I with (resolution: FWHM $=1.76$ arcsec) and the *HST* I data for a 4×3 arcsec region 6.5 arcsec east of the nucleus. This object was spectroscopically identified as an H II region and designated knot A by Wakamatsu & Nishida (1980), and is a strong source of Hα in the map of Pogge (1989). Our I-band

contour map shows that this star cluster contains four components. The brightest contains 70% of the knot A flux within an ellipse 0.19×0.25 arcsec (10×13 pc, assuming $D=10$ Mpc).

Using the unsharp masked image (Fig. 3) to identify the star clusters, we measured the locations, integrated magnitudes, and diameters of 14 within the nuclear ring. The star cluster parameters listed in Table I are derived from the Lucy deconvolved data shown in Fig. 2. The diameters are effective isophotal diameters ($D=2*\sqrt{A/\pi}$, where $A=$area within the $\mu_I=17.4$ isophote). The brightnesses are integrated fluxes within the $\mu_I=17.4$ isophote, corrected for pixel size and calibrated using the relationship shown in Fig. 4. The positions are derived from the geometric mean within the $\mu_I=17.4$ isophote.

Purely as an additional confirmation of the resolution of these data (Fig. 2), we show that the sizes of the star clusters in NGC 4314 are distributed according to

$$N=N_0 e^{-D/D_0},$$

where N is the number of emission regions larger than D. This is shown in Fig. 10, a plot of I diameters in pc vs $\log N$. The best fit, neglecting the largest H II region (identified as knot B in Wakamatsu & Nishida 1980), gives $N_0=21.8\pm1.5$, and $D_0=18.2\pm0.7$ pc. The relationship prevails down to 7 pc, which argues that we are achieving at least 0.14 arcsec resolution.
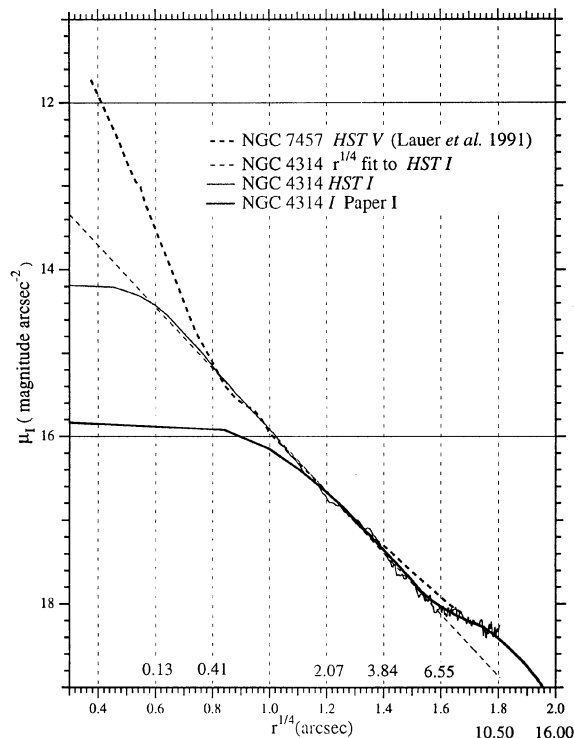
NGC 4314 *vs* NGC 7457 $r^{1/4}$ Profiles

FIG. 8. We compare the $r^{1/4}$ profiles for NGC 7457 and NGC 4314. The NGC 7457 V-band profile has been shifted arbitrarily in magnitude. Compared to NGC 7457, NGC 4314 has no central cusp.

TABLE 1. NGC 4314 star clusters.

ID	integrated magnitude (I-band)	diameter (arcsec)	diameter (pc)	Positional Offset x (arcsec)	y (arcsec)	
1	16.82	1.04	50.5	0.52	-4.95	knot B
2	18.08	0.76	37.0	-6.28	0.13	knot A
3	18.22	0.70	34.0	-2.32	4.39	
4	18.77	0.69	33.7	5.03	4.82	
5	19.15	0.54	26.1	4.30	5.72	
6	19.24	0.51	24.6	-3.48	-5.46	
7	19.70	0.43	20.6	4.43	-1.85	
8	19.85	0.41	20.1	3.57	5.89	
9	20.01	0.38	18.5	5.85	2.92	
10	20.32	0.38	18.2	5.50	3.83	
11	20.53	0.28	13.7	-5.50	-0.34	
12	21.32	0.22	10.5	6.24	2.41	
13	21.49	0.19	9.1	6.11	2.02	
14	22.03	0.15	7.1	0.56	5.89	

Notes to TABLE 1
Positional offsets are referenced to an I-band photocenter of
RA = 12h 22m 31.983s,   DEC = +29° 53' 44.23" (2000.0)
Positional errors: ±0.05 arcsec relative, ±0.2 arcsec absolute.

4314. The dust lanes, resolved into a clear spiral pattern of clumps, seem to support orbit orientation crowding causing collisions between clouds which instigate star formation (Combes 1988). The likely identification of bar_2 supports the possibility that a spiral pattern, driven by a nuclear bar potential, could cause new star formation in a spiral shaped distribution.

A deconvolved *HST* I-band image of the nucleus of NGC 4314 resolves individual star clusters associated with a nuclear ring of H II regions. The distribution of dust follows a clear spiral pattern. The largest clouds appear to be associated with the largest star clusters. Evidence from the distribution of star cluster sizes and the $r^{1/4}$ profile suggests that the resolution of the deconvolved data lies very near 0.14 arcsec. Lucy–Richardson deconvolution is an effective and flux-conserving technique for partially repairing the damage done by spherical aberration to *HST* data.

Unlike results from similar *HST* data on NGC 7457 and M87 (Lauer *et al.* 1992), we find no evidence for a stellar cusp in the center of NGC 4314. We have collected

6. CONCLUSIONS

These data have provided a few new observational constraints and clues as to which star formation mechanism discussed in Paper I is operating in the nucleus of NGC

Knot A: *HST vs.* the Ground

FIG. 9. Contour maps from data discussed in Paper I (MCD I) and the *HST* data discussed in this paper (*HST I*) presented at the same scale. The peak contour in the *HST* map is $\mu_I = 16.5$. $\Delta m = 0.10$. This object is Wakamatsu & Nishida (1980) knot A.

NGC 4314 Nuclear Ring Integral Frequency Distribution of Star Cluster Diameters

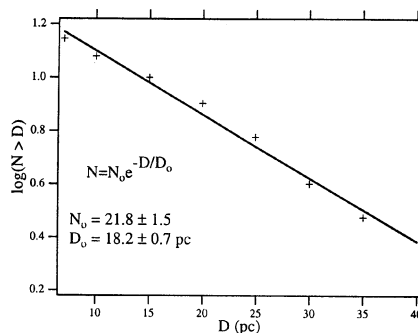FIG. 10. Integral frequency distribution of star cluster diameters. The size distribution is exponential and prevails down to 7 pc=0.14 arcsec. Diameters are isophotal within $\mu_I \leqslant 17.4$ and are measured from the deconvolved data displayed in Fig. 2.

evidence for another barlike stellar distribution in addition to bar$_1$, the bar prominent on the POSS prints. These *HST* data present us with bar$_2$, a 8 arcsec length bar parallel to bar$_1$. Recent star formation may be associated with the ends of bar$_2$. A 2 arcsec length nuclear bar discussed in Paper I is not confirmed and may be an artifact. We find that the star clusters associated with the H II regions obey an exponential integral size distribution.

These data demonstrate the potential of *HST* for surface photometry of galaxies. After the planned mainte-nance and refurbishment mission (late 1993) we will obtain *B*, *V*, *R*, *I*, and Hα data with the next generation wide-field camera, which will correct the *HST* spherical aberration.

REFERENCES

Benedict, G. F., Higdon, J. L., Tollestrup, E. V., Hahn, J., & Harvey, P. M. 1992, AJ, 103, 757 (Paper I)

Bessel, M. S. 1979, PASP, 91, 589

Burrows, C. J., Holtzman, J. A., Faber, S. M., Bely, P. Y., Hasan, H., Lynds, C. R., & Schroeder, D. 1991, ApJ, L21

Combes, F. 1988, in Galactic & Extragalactic Star Formation, edited by E. Pudritz and M. Fich (Kluwer, Dordrecht), p. 475

Combes, F., & Gerin, A. 1985, A&A, 150, 327

Combes, F., Gerin, A., Nakai, N., Kawabe, R., & Shaw, M. A. 1992, A&A, 259, L27

Garcia-Barreto, J. A., Downes, D., Combes, F., Gerin, M., Magri, C., Carrasco, L., & Cruz-Gonzalez, I. 1991, A&A, 244, 257

Griffiths, R. 1990, WFPC Instrument Handbook, Version 2.1 (ST ScI, Baltimore)

Jedrzejewski, R. 1987, MNRAS, 226, 747

Lauer, T. 1989, PASP, 101, 445

Lauer, T. 1992, private communication

Lauer, T., et al. 1991, ApJ, 369, L41

Lauer, T., et al. 1992, AJ, 103, 703

Lucy, L. B. 1974, AJ, 79, 745

Pogge, R. W. 1989, ApJS, 71, 433

Teuben, P. J., & Sanders, R. H. 1985, MNRAS, 212, 257

Wakamatsu, K., & Nishida, M. T. 1980, PASJ, 32, 389